An active core-shell nanoscale design for high voltage cathode of lithium storage devices

Zhongpei Lu[1], Yang Liu[1], Xiaojun Lu[1], Hao Wang[1], Gang Yang[1*], Yimin Chao[2*], Fan Yin[1], Weili Li, and Xuefan Jiang[1]

[1] Jiangsu Laboratory of Advanced Functional Material, School of Chemistry and Materials Engineering, Changshu Institute of Technology, Changshu 215500, P. R. China

[2] Energy Materials Laboratory, School of Chemistry, University of East Anglia, Norwich NR4 7TJ, UK

* To whom correspondence should be addressed:

   E-mail: gyang@cslg.edu.cn (GY)
           y.chao@uea.ac.uk (YC)

Abstract: Spinel $LiNi_{0.5}Mn_{1.5}O_4$ (LNM) is a potential high-voltage cathode for commercial lithium-ion batteries (LIBs). Maintaining an appropriate amount of Mn^{3+} in LNM is necessary to improve the rate performance. However, Mn^{3+} dissolution in the interface of LNM and electrolyte leads to the fast capacity degradation. Therefore, designing a cathode to prevent Mn^{3+} loss during charge/discharge is important for high performance LIBs. Here we present an active core-shell design with coating another high-voltage cathode material $LiCoPO_4$ (LCP) on the surface of LNM nanoparticles. The LCP layer can simultaneously induce Mn^{3+} ions at the interface between LCP and LNM, and act as a stable shell to prevent the loss of Mn^{3+}. The optimized sample LNM@5%LCP possesses 128 mAh g^{-1} at 0.5 C and 115 mAh g^{-1} at 20 C rate, and maintains 96% of the initial capacity operated at 55°C over 100 cycles.

High-performance lithium-ion batteries (LIBs) have been developed into promising energy storage devices for electric vehicles (EVs), hybrid electric vehicles (HEVs), and portable electronic devices[1,2]. Significant progresses have been made on materials for cathode, which is still one of the shortcomings in electric vehicle applications[3,4]. In recent years, high-voltage spinel $LiNi_{0.5}Mn_{1.5}O_4$ is considered as one of the most potential cathode materials for LIBs. $LiNi_{0.5}Mn_{1.5}O_4$ has a voltage plateau at 4.7 V, making the energy density up to 650 Wh kg^{-1}, which is much higher than those in other cathode materials such as $LiCoO_2$ (~ 460 Wh kg^{-1}), $LiMn_2O_4$ (~ 400 Wh kg^{-1}), $LiFePO_4$ (~ 495 Wh kg^{-1}), $LiNi_{0.5}Co_{0.3}Mn_{0.2}O_2$ (~ 550 Wh kg^{-1}), and $LiNi_{1/3}Co_{1/3}Mn_{1/3}O_2$ (~ 576 Wh kg^{-1}) [5-8].

$LiNi_{0.5}Mn_{1.5}O_4$ is usually with two types of structures: ordered and disordered. The ordered spinel (P $4_3$32) is well ordered in two distinct octahedral sites, 4b sites for Ni(2+) and 12d sites for Mn(4+). The disordered spinel (Fd-3m) includes Ni(2+)/Mn(4+) randomly distributed in 16d octahedral sites or the presence of Mn(3+).[9,10] An appropriate amount of Mn^{3+} ions is one of the sensitive factors improving the electrochemical properties of $LiNi_{0.5}Mn_{1.5}O_4$[11-14]. Mn^{3+} ions in disordered spinel can increase the conductivity to approximately two orders of magnitude higher than that of ordered spinel[11], although the rate performance of the spinel is not directly proportional to the Mn^{3+} content[15]. However, Mn^{3+} in disordered spinel leads to a side reaction that produces soluble Mn^{2+} dissolved in the electrolyte and causes significant capacity loss during cycling, especially at elevated temperatures[16].

An appropriate amount of Mn^{3+} ensures the high rate performance of $LiNi_{0.5}Mn_{1.5}O_4$, but the dissolution of Mn^{3+}/Mn^{2+} results in the serious capacity fading. In order to resolve the contradictions, two interesting routes have been explored in surface modification to prevent the loss of Mn^{3+} and also prevent the oxidation of the electrolyte operated at very high voltage. The first one is forming cathode film during charging/discharging processes[17,18]. For example,

Cresce *et al* reported a surface modification was used to decrease the aggressive side reaction of spinel occurred during sustained 4.7 V operation or in elevated temperature[17]. Xu *et al* reported an effect way that a novel electrolyte system utilizes additives for designed surface modification to generate a cathode passivation layer[18]. The second route is directly coating inorganic materials on $LiNi_{0.5}Mn_{1.5}O_4$ during the step of material preparation, such as Bi_2O_3, Al_2O_3, SiO_2, $AlPO_4$[18-22]. Konishi *et al* build a stable functional protecting layer of Li_3PO_4 on the surface of $LiNi_{0.5}Mn_{1.5}O_4$, which shows improved cycle performance[21]. Kim studied the effects of depositing ultrathin (<1 nm) Al_2O_3 layers on $LiNi_{0.5}Mn_{1.5}O_4$ particles using atomic layer deposition. The coating layer of Al_2O_3 was significantly improving columbic efficiency and cycle performance through suppressing the self-discharge and dissolution of transition metals[18]. Gottfried's group reported a $Li_4Ti_5O_{12}$ film was coated as buffer layer onto a $LiNi_{0.5}Mn_{1.5}O_4$. Because Mn and Ni in the near-surface region diffused from the $LiNi_{0.5}Mn_{1.5}O_4$ layer into the coating layer of $Li_4Ti_5O_{12}$, the cycle performance of $Li_4Ti_5O_{12}$ coated $LiNi_{0.5}Mn_{1.5}O_4$ is still poor, 102 mAh g^{-1} at the 1st cycle and only 60 mAh g^{-1} at the 100th cycle[22].

Considering both high rate performance and high reversibility for lithium storage of 4.7 V cathode $LiNi_{0.5}Mn_{1.5}O_4$, the coating material should play the roles in tuning the amount of Mn^{3+} and constructing an stable shell on $LiNi_{0.5}Mn_{1.5}O_4$ to prevent the loss of Mn^{3+}. Here we choose $LiCoPO_4$, another 4.7 V cathode, as a stable shell for spinel, with the hypothesis that its inorganic nature and excellent chemical stability up to 4.7 V with organic electrolyte ensure a durable surface protection for LNM at high voltage. Olivine $LiCoPO_4$, a polyanion material, is reported to have theoretical specific capacity of 170 mAh g^{-1} at a discharge plateau near 4.8 V[23-26]. The growth of $LiCoPO_4$ as coating layer is to induce the appearance of Mn^{3+} in $LiNi_{0.5}Mn_{1.5}O_4$ during the synthesis; moreover $LiCoPO_4$ thin layer can contribute to enhancing capacity by utilizing nanosized particles[27-29].

In this work, a spherical core-shell structure of high-voltage cathode material with $LiNi_{0.5}Mn_{1.5}O_4$ (core) and $LiCoPO_4$ (shell) is designed and a series of composites LNM@x%LCP (x = 1, 5, 10 weight ratio) has been synthesized by one-pot hydrothermal method. The optimized sample LNM@5%LCP has achieved a reversible capacity 128 mAh g^{-1} at 0.5 C and 115 mAh g^{-1} at 20 C rate (1 C = 150 mAh g^{-1}). Furthermore, even operated at 55 °C for 100 cycles, 96% of the initial capacity has been retained with sample LNM@5%LCP. The results have successfully demonstrated that $LiCoPO_4$ shell plays the following important roles: (1) inducing Mn^{3+} between the interface of $LiNi_{0.5}Mn_{1.5}O_4$ and $LiCoPO_4$, (2) preventing Mn^{3+} dissolution during charge and discharge cycles, (3) inhibiting the decomposition of electrolyte $LiPF_6$ due to the common-ion effect.

Results and Discussion

Synthesis of LNM@x%LCP. Schematic preparation procedure for $LiCoPO_4$ coated $LiNi_{0.5}Mn_{1.5}O_4$ is shown in Figure 1. The as-produced $LiNi_{0.5}Mn_{1.5}O_4$ sample is consistent of porous spherical micrometer scale particles. Each spherical LNM particle is composed by ordered self-assembled nanocrystals and full of flowable space. The facile hydrothermal method is employed to prepare LNM@x%LCP because the abundant flowable space within the porous structure of LNM is conducive for the transportation of the ions of Li^+, Co^{2+} and PO_4^{3-} to produce $LiCoPO_4$ shell coated on the primary nanocrystals of $LiNi_{0.5}Mn_{1.5}O_4$.

The SEM and TEM images of LNM@5%LCP spherical particles show the surface morphology and the sectional views after the particles crashed into half (Figure 1a-1f). LNM@5%LCP samples present homogeneous spherical morphologies with particle diameters in the region of 5-8 μm (Figure 1a). Each spherical micrometer scale particle is covered by numerous nanoparticles of diameter ~ 80 nm (Figure 1b and Figure S1 in Supplementary). From the sectional view of LNM@5%LNM, one can see that the spherical micrometer particle is porous and full of flowable space (Figure 1c and 1d). The porous spherical

morphologies are also presented in samples of LNM@1%LCP and LNM@10%LCP (Figure S2 in Supplementary). The porous structure of spherical $LiNi_{0.5}Mn_{1.5}O_4$ is useful for the efficient contact with electrolyte and providing the channels for lithium diffusion during charge/discharge processes. TEM images show the tough surface of a LNM@5%LCP particle (Figure 1e), and a very thin LCP coating layer is visible on the surface of primary LNM particle (in Figure 1f).

The elemental distribution and composition on the surface and cross-section of LNM@5%LCP are analyzed by energy dispersive spectroscopy (EDS) shown in Figure 2, where Ni, Mn, Co and P can be identified clearly. The distribution of Co and P are complete and uniform on the particle surface and all over the cross-section of LNM@5%LCP particles, indicating a homogeneous formation of nano-LCP coating layer. Similar results from LNM@1%LCP and LNM@10%LCP are also observed, as shown in Figure S3 in Supplementary.

The powder XRD patterns of the pure $LiNi_{0.5}Mn_{1.5}O_4$ and the composites LNM@1%LCP, LNM@5%LCP, and LNM@10%LCP are displayed in Figure 3. All the peaks in the XRD patterns are well matched with $LiNi_{0.5}Mn_{1.5}O_4$ phase (JCPDS 80-2162). The enlarged XRD patterns (the inset in Figure 3) show weak characteristic peaks of $LiCoPO_4$ (JCPDS 32-0552) indexed by (101) at 22.4° and (020) at 30.8° from samples LNM@5%LCP and LNM@10%LCP[30]. The ICP and specific surface area for the samples are summarized in Table 1. The absolute moles of Mn and Ni elements in pure LNM and composites LNM@x%LCP are all resided within proper range from ICP results and the amounts of Co and P are changed concurrently with the stated quantity of $LiCoPO_4$ (Table 1). Owing to similar porous spherical morphologies appeared in the four samples, the specific surface area values are very close, 6.67 m^2 g^{-1} in pure LNM, 5.89, 5.22 and 4.80 m^2 g^{-1} in LNM@1%LCP, LNM@5%LCP and LNM@10%LCP, respectively.

Mn^{3+} on the spinel induced by $LiCoPO_4$ shell. The residual amount of Mn^{3+} in spinel $LiNi_{0.5}Mn_{1.5}O_4$ is one of the important factors affecting the rate and cyclic performance[11-14]. In this work, Mn^{3+} in the starting spinel $LiNi_{0.5}Mn_{1.5}O_4$ is reduced to a very low value through re-annealing at 700°C for 10 hours (Table 1), but a considerable amount of Mn^{3+} in $LiNi_{0.5}Mn_{1.5}O_4@x\%LiCoPO_4$ has been detected by initial discharge profiles and XPS measurement, respectively.

A characteristic discharge plateau at 4.0 V is a sensitive index to estimate the sum content of Mn^{3+} in the spinel $LiNi_{0.5}Mn_{1.5}O_4$[11,14,31]. The sum of Mn^{3+} in pure LNM, LNM@1%LCP, LNM@5%LCP and LNM@10%LCP is 0, 1.05%, 6.31% and 10.86%, respectively (listed in Table 1), according to the capacity contribution from 4.0 V discharge plateau (Figure S4 in Supplementary). The sum of Mn^{3+} observed in $LiNi_{0.5}Mn_{1.5}O_4@x\%LiCoPO_4$ increases concurrently with the increasing amount of $LiCoPO_4$ shell.

It is well known that XPS is a powerful method to study the elemental state located on the crystal surface. The high resolution Co2p spectra (Figure S5a in Supplementary) show a strong peak at binding energy of 781 eV, which can be attributed to Co^{2+} in $LiCoPO_4$, and P2p (Figure S3b in Supplementary) observed at 133.5 eV corresponds to the P^{5+} state in $LiCoPO_4$ [35]. The high resolution XPS peaks in the region of Mn2p prove the mixed states of Mn^{3+} and Mn^{4+} in the samples as shown in Figure 4. According to the fittings, the surface Mn^{3+} in LNM, LNM@1%LCP, LNM@5%LCP and LNM@10%LCP is calculated about 18.1%, 27.0%, 34.9% and 45.8% of the total amount of Mn element detected on the surface by XPS, respectively (Table 1). The percentages of Mn^{3+} recorded by XPS give the same trend increasing with the amount of $LiCoPO_4$, but the values of Mn^{3+} are much higher than those calculated by 4.0 V plateau. Mn^{3+} of spinel induced by $LiCoPO_4$ shell might be mainly existed in the interface between $LiCoPO_4$ and $LiNi_{0.5}Mn_{1.5}O_4$ phases, but the reason why Mn^{3+} on spinel can be induced by $LiCoPO_4$ is still unknown. In order to understand the oxidation states further, the

high resolution XPS spectra in the region of Mn3s taken on LNM, LNM@1%LCP, LNM@5%LCP, LNM@10%LCP, respectively, are displayed in Figure S6. The splitting between Mn3s peak and its satellite is related with the chemical state of Mn element. The average oxidation state (AOS) of Mn^{+AOS} can be calculated by the following equation[34,35]:

$$AOS = 8.956 - 1.126 \triangle E \qquad (1)$$

where $\triangle E$ is the splitting energy in the peak fitting for Mn3s. The calculated AOS values are 4.03, 3.99, 3.88 and 3.79 for pure LNM, LNM@1%LCP, LNM@5%LCP and LNM@10%LCP, respectively.

Cyclic voltammetry (CV) profile is another technique to demonstrate the appearance and amount of Mn^{3+} in LNM. Figure 5 shows the redox processes of pure LNM and the composites LNM@x%LCP. In the CV curve of pure LNM, only one pair of redox peaks are presented at the potentials of 4.65/4.83 V, which are associated with the oxidation/reduction of Ni^{2+}/Ni^{4+} (Figure 5a). After LCP coating, a couple of extra peaks near 4.0 V are clearly appeared in the composites, which are "fingerprint peaks" of the redox related with Mn^{3+}, 4.02/3.97 V in LNM@5%LCP and 4.04/3.97 V in LNM@10%LCP. It is worth noting that the peaks close to 4.0 V related with Mn^{3+} become stronger and stronger along with the increased amount of $LiCoPO_4$. It is the evidence that Mn^{3+} is induced by $LiCoPO_4$ shell and changes concurrently with the amount of $LiCoPO_4$. Moreover, the peaks close to 4.8/4.6 V are split to double features, which are assigned to Ni^{2+}/Ni^{3+} and Ni^{3+}/Ni^{4+} respectively, because the conductivity of LNM is increased upon the appearance of Mn^{3+}.

Electrochemical properties. The schematic interface structure of $LiNi_{0.5}Mn_{1.5}O_4@LiCoPO_4$ is shown in Figure 6a. While spherical particles of LNM@ x%LCP as cathode adhered to current collector using the polymeric binder of PVDF, $LiCoPO_4$ shell has direct contact with electrolyte (EL), which has hindered the dissolution of Mn^{3+} from spinel. The following four components are involved in the composite LNM@x%LCP: (1) the interface between

electrolyte (EL) and LiCoPO$_4$, (2) the shell of LiCoPO$_4$ phase, (3) the interface between LiCoPO$_4$ and LiNi$_{0.5}$Mn$_{1.5}$O$_4$, and (4) the core of LNMO phase. Lithium ions insertion and extraction have to go through them and different electrochemical performances are presented in the samples of LNM@1%LCP, LNM@5%LCP and LNM@10%LCP, respectively. Electrochemical impedance spectra (EIS) and the relative fitting by equivalent circuit are powerful methods to simulate the electrochemical properties. The EIS of LNM@1%LCP, LNM@5%LCP and LNM@10%LCP are plotted in Figure 6b and the fitted parameters are listed in Table S2. The equivalent circuits are proposed for the microstructures of LNM@ x%LCP in Figure 6c. R_s is the solution resistance of a cell, with a similar value in the three samples of LNM@ x%LCP. R_p, the polarization resistance of Li ions through the interface between electrolyte (liquid) and LiCoPO$_4$ (solid), is increased concurrently with the amount of LiCoPO$_4$ shell, 66.35 ohms in LNM@1%LCP, 197.4 ohms in LNM@5%LCP and 202.6 ohms in LNM@10%LCP, respectively, in line with the intrinsic poor conductivity of LiCoPO$_4$. R_{ct}, the charge transfer resistance happened at LiCoPO$_4$ layer, is also increased concurrently with the amount of LiCoPO$_4$ shell. $R_{p'}$, the resistance of lithium ions through the interface between LiCoPO$_4$ shell and LiNi$_{0.5}$Mn$_{1.5}$O$_4$ core, is in the same magnitude in the three samples because the existences of Mn^{3+} in the three samples render a good conductivity. $Z_{w (LCP)}$ and $Z_{w (LNM)}$ are the Warburg resistances of lithium ions transporting through LiCoPO$_4$ shell and LNM core. Because the intrinsic conductivity of LiCoPO$_4$ is much poorer than that of LiNiPO$_4$, $Z_{w (LCP)}$ is much higher than $Z_{w (LNM)}$.

GITT technique based on chronopotentiometry directly reflects the diffusion ability of Li$^+$ during charge and discharge[36]. The D_{Li^+} values of pure LNM and composites of LNM@ x%LCP are calculated and plotted in Figure 6d-f. The lowest D_{Li^+} of each sample is appeared in the phase change of Ni^{2+}/Ni^{4+}. At 4.7 V, the D_{Li^+} values of pure LNM and LNM@1%LCP

are much lower than those of LNM@5%LCP and LNM@10%LCP, confirming a certain amount of Mn^{3+} in the samples effectively improve the diffusion ability of Li^+.

The initial specific capacities and cyclic stability of pure LNM, LNM@1%LCP, LNM@5%LCP and LNM@10%LCP as cathode operated at 25 °C and 55 °C, are compared in Figure 7. Pure LNM and LNM@1%LCP deliver the initial capacities of 141 and 136 mAh g^{-1} at 0.5 C rate, higher than 128 mAh g^{-1} in LNM@5%LCP and 112 mAh g^{-1} in LNM@10%LCP (Figure 7a). The sample LNM@10%LNM, with highest amount of $LiCoPO_4$, shows lowest initial specific capacity due to the intrinsic low conductivity of $LiCoPO_4$. As shown in Figure S7 in Supplementary, the initial capacity is only 51 mAh g^{-1} for pure $LiCoPO_4$. All the three samples give a 4.7 V discharge plateau, which is attributed to the redox of Ni^{2+}/Ni^{4+}. The other plateau near 4.0 V is observed corresponding to the "fingerprint" plateau reflected the redox reaction between the Mn^{3+} and Mn^{4+} couple. The 4.0 V plateau of the composite is another evidence that the amount of Mn^{3+} in spinel is concurrently increased with the increased amount of $LiCoPO_4$ shell. Figure 7b shows the cyclic stability of the samples. After 100 charge/discharge cycles, pure LNM and LNM@1%LCP exhibit rapid capacity loss, only 58 % and 64 % of their initial capacity are remained, respectively. However, both samples LNM@5%LCP and LNM@10%LCP show excellent cyclic stability, 96% and 95% of their initial capacity are remained, respectively. At elevated temperature of 55 °C, LCP shell plays even more important role in maintaining electrochemical performance of LNM@ x%LCP samples (see Figure 7c and 7d). At the 100th cycle, only 64 % of its initial discharge capacity is remained in LNM@1%LCP, but LNM@5%LCP with the preferred shell presents the best performance, 96 % of its initial discharge capacity (120.9 mAh g^{-1}) is maintained. It can be concluded that $LiCoPO_4$ shell does play a key role in ensuring the cyclic stability of LNM@ x%LCP samples.

As mentioned above, the other important role of $LiCoPO_4$ is to induce the appearance of Mn^{3+}, which is useful in improving rate performance of LNM. Figure 8 shows the rate cyclic performance of the samples operated from 0.5 C to 20 C rate. At 20 C rate, LNM@5%LCP delivers the initial capacity of 115 mAh g^{-1} (Figure 8a), which is the highest value in comparison with 57 mAh g^{-1} of pure LNM, 87 mAh g^{-1} of LNM@1%LCP, and 92 mAh g^{-1} of LNM@10%LCP. The polarization of LNM@5%LCP electrode is the smallest within these four samples. It is observed that the rate capability of LNM@5%LCP is far better than other samples (Figure 8b and 8c). Ragone plots of the four samples are shown in Figure 8d. The inverse relationship between specific energy density and specific power density is well established. Remarkably, LNM@5%LCP electrode delivers a gravimetric energy density of 475.1 Wh kg^{-1} while delivering a power density of 13.2 KW kg^{-1}, much better than other samples.

The state of electrode and electrolyte after charge and discharge cycles. It is reported in literature that the $LiPF_6$ of electrolyte worked at high voltage might be decomposed and deposited on electrode materials[37-39]. In order to analyze the surface changes of active materials, XPS spectra on the electrodes with pure LNM, LNM@1%LCP, LNM@5%LCP and LNM@10%LCP charged/discharged after 100 cycles at 20 C rate have been collected, see Figure 9. The P2p spectrum taken on the pure LNM electrode is clearly identified as two strong components (Figure 9a), Li_xPF_y at ~137.5 eV and $Li_xPO_yF_z$ at ~ 134.5 eV, respectively. This is consistent with the previous studies that an unwanted decomposition of the standard electrolyte, $LiPF_6$, always happens on the surface of cathode with operating potentials over 4.5 $V^{20,39,41}$. For the cycled electrode of LNM@1%LCP, the minor P state is from Li_xPF_y and the major P state is phosphate from the shell of $LiCoPO_4$ (Figure 9b). For the both cycled electrodes of LNM@5%LCP and LNM@10%LCP, the P state from Li_xPF_y is hardly to be detected (Figure 9c and 9d). It is clearly concluded that the P state from PF_6^- in the electrodes

of LNM@ x%LCP is dramatically reduced with the increasing amount of LiCoPO$_4$ shell. The percentages of P state of Li$_x$PF$_y$ are 4.86%, 0.05% and 0.03% of the total P detected in LNM@1%LCP, LNM@5%LCP and LNM@10%LCP, respectively. It is evidenced that LiCoPO$_4$ shell plays the roles in avoiding unwanted decomposition of electrolyte and improving the cyclic ability of LiNi$_{0.5}$Mn$_{1.5}$O$_4$ operated at high voltage.

Conclusion

A novel series of composites LiNi$_{0.5}$Mn$_{1.5}$O$_4$@ x%LiCoPO$_4$ (LNM@ x%LCP) have been synthesized and investigated as 4.7 V cathode for LIBs. LiCoPO$_4$ (LCP) as shell has been grown on the surface of LiNi$_{0.5}$Mn$_{1.5}$O$_4$ (LNM) particles under hydrothermal condition. The growth of LCP has simultaneously induced Mn^{3+} on the interface of LCP and LNM, and the amount of Mn^{3+} increases with the growth of LCP shell. The appearance of Mn^{3+} has dramatically improved the conductivity and lithium diffusion ability of LNM. The sample LNM@5%LCP has shown the best electrochemical properties, 128 mAh g^{-1} at 0.5 C rate and 96 % of its initial capacity remained after 100 cycles. At 20 C rate, LNM@5%LCP has demonstrated the best performance of 115 mAh g^{-1}, much higher than 57 mAh g^{-1} of pure LNM. It can be concluded that an appropriate amount of Mn^{3+} is necessary for improving the capacity and rate performance, while the stable shell of LCP ensures the excellent cyclic stability of LNM@5%LCP owing to its preventing the dissolution of Mn^{3+}. It is worth noting that LiCoPO$_4$ as a stable shell effectively reduces the decomposition of the electrolyte LiPF$_6$ as well. The construction of active core@ stable shell is simple and applicable in preparing electrode materials for high-performance LIBs.

Methods

Synthesis of LiNi$_{0.5}$Mn$_{1.5}$O$_4$@LiCoPO$_4$ nanoparticles. LiNi$_{0.5}$Mn$_{1.5}$O$_4$@LiCoPO$_4$ was synthesized using one-pot hydrothermal method. Spherical LiNi$_{0.5}$Mn$_{1.5}$O$_4$ particles as core were produced by co-precipitation (See details in Supplementary). LiNi$_{0.5}$Mn$_{1.5}$O$_4$ particles

were well dispersed in an aqueous solution of $Co(NO_3)_2 \cdot 6H_2O$ and H_3PO_4. After vigorous stirring for 2 h, aqueous LiOH solution in the molar ratio of Li : Co : P set 2.0 : 1.0 : 1.0 was placed into the mixture. The pH value of the mixture was adjusted to 8.5 by using ammonia. The final suspension was transferred into an autoclave and reacted for 10 h at 200 °C. The black precipitate was centrifuged, washed for several times with distilled water and absolute ethyl alcohol, and finally dried at 60 °C. In order to improve the crystallinity of $LiCoPO_4$ shell, the precipitate was annealed at 700 °C for 10 h under air atmosphere. The as-synthesized composites with starting mass ratio of $LiCoPO_4$ at 1 %, 5 % and 10 % of $LiNi_{0.5}Mn_{1.5}O_4$ in theoretical values, are simply named as LNM@1%LCP, LNM@5%LCP and LNM@10%LCP, respectively. The real mass ratios of $LiCoPO_4$ in the final composites were measured by ICP considering the yield of $LiCoPO_4$ in hydrothermal condition. To study the morphologies, elemental state of the electrode and electrolyte decomposition after hundreds of charge/discharge cycles, cells were disassembled in an Ar-filled glove box. The components were rinsed for several times with dimethyl carbonates (DMC). The cathode was dried in Ar-filled glove box overnight prior to the XPS analysis.

Characterization. X-ray diffraction (XRD) measurements were carried out with a Rigaku diffractometer (Dmax-2200, Cu Ka radiation). A field-emission scanning electron microscope (FE-SEM, SIGMA, ZEISS, 20kV), and a transmission electron microscope (TEM, JEOL-2000CX, 200 kV and HRTEM, JEOL-2010F, 200 kV) were employed to analyze the morphologies of samples. The composition and elemental state of the samples were analyzed by inductively coupled plasma (ICP) and X-ray photoelectron spectroscopy (XPS-ULVAC-PHI PHI 5000 Versa Probe spectrometer, Al Ka radiation, hv = 1486.6 eV).

Electrochemical test. Electrochemical performances of as-prepared samples were measured using CR2016 coin cells. The working electrode was a mixture of 80 wt% as-synthesized sample, 10 wt% acetylene black, and 10 wt% polyvinylidene difluoride binder in N-methyl

pyrrolidinone solvent. The slurry was casted on aluminum foil with mass loading of *ca* 3 mg cm^{-2}, and dried at 100°C for 12 h under vacuum. The half-coin cell was assembled in an argon-filled glove box, using lithium metal as anode, Celgard 2500 as the separator, and 1 M LiPF$_6$ dissolved in ethylene carbonate and ethyl methyl carbonate (1 : 1 volume ratio) as the electrolyte. The assembled cell was galvanostatically cycled between 3.0 to 5.0 V at various current rates ranging from 0.5 to 20 C (1 C = 150 mAh g^{-1}) by a LAND CT2001A battery test system. The working temperature for cell's cycling test was set at 25 °C and 55 °C, respectively. All of the specific capacities were calculated on the basis of total mass of LiNi$_{0.5}$Mn$_{1.5}$O$_4$@LiCoPO$_4$. Galvanostatic intermittent titration technique (GITT) was conducted at room temperature in the voltage range of 3.0-5.0 V. Cyclic voltammetry (CV) tests were carried on PARSTAT2273 electrochemical workstation at the scanning rate of 0.1 mV s^{-1} in the potential ranges from 3.0 to 5.0 V (vs. Li$^+$/Li). Electrochemical impedance spectroscopy (EIS) measurement was carried out by using PARSTAT2273 electrochemical workstation range from 100 kHz to 10 mHz with sinusoidal signal of 5 mV.

Author contributions

G.Y. conceived the project. Z.P.L., Y.L., X.J.L. and G.Y. designed the experiments. C.F.D., H.W., Y.C., F.Y. and X.F.J. synthesized the samples, performed the experiments and analyzed the data. Z.P.L., Y.L., G.Y. and Y.C. wrote the manuscript.

References

[1] Larcher, D. & Tarascon, J-M. Towards greener and more sustainable batteries for electrical energy storage. *Nat. Chem.* **7,** 19−29 (2015).

[2] Tang, Y. X., Zhang, Y., Li, W. L., Ma, B. & Chen, X. Rational material design for ultrafast rechargeable lithium-ion batteries. *Chem. Soc. Rev.* **44,** 5926−5940 (2015).

[3] Andre, D. et al. Future generations of cathode materials: an automotive industry perspective. *J. Mater. Chem. A* **3,** 6709−6732 (2015).

[4] Fan, X. et al. Pomegranate-structured conversion-reaction cathode with a built-in Li source for high-energy Li-ion batteries. *ACS Nano* **10,** 5567–5577 (2016).

[5] Zhao, M. et al. Diphenyl disulfide as a new bifunctional film-forming additive for high-voltage $LiCoO_2$/graphite battery charged to 4.4V. *J. Power Sources* **323,** 29−36 (2016).

[6] Yang, X. et al. High-performance aqueous asymmetric supercapacitor based on spinel $LiMn_2O_4$ and nitrogen-doped graphene/porous carbon composite. *Electrochim. Acta* **180,** 287−294 (2015).

[7] Tian, R. et al. Drastically enhanced high-rate performance of carbon-coated $LiFePO_4$ nanorods using a green chemical vapor deposition (CVD) method for lithium ion battery: A selective carbon coating process. *ACS Appl. Mater. Interfaces* **21,** 11377−11386 (2015).

[8] Patoux, S. et al. High voltage spinel oxides for Li-ion batteries: From the material research to the application. *J. Power Sources* **189,** 344−352 (2009).

[9] Chemelewski, K. R. & Manthiram, A. Origin of site disorder and oxygen nonstoichio-metry in $LiMn_{1.5}Ni_{0.5-x}M_xO_4$ (M = Cu and Zn) cathodes with divalent dopant ions. *J. Phys. Chem. C* **117,** 12465–12471 (2013).

[10] Xiao, J. el al. Interplay between two-phase and solid solution reactions in high voltage spinel cathode material for lithium ion batteries. *J. Power Sources* **242,** 736–741 (2013).

[11] Xiao, J. et al. High- performance $LiNi_{0.5}Mn_{1.5}O_4$ spinel controlled by Mn^{3+} concentration and site disorder. *Adv. Mater.* **24,** 2109−2116 (2012).

[12] Jafta, C. J., Mathe, M. K., Manyala, N., Roos, W. D. & Ozoemena, K. I. Microwave-assisted synthesis of high-voltage nanostructured $LiNi_{0.5}Mn_{1.5}O_4$ spinel: tuning the Mn^{3+} content and electrochemical performance. *ACS Appl. Mater. Interfaces* **5,** 7592–7598 (2013).

[13] Gao, P. et al. Microwave rapid preparation of $LiNi_{0.5}Mn_{1.5}O_4$ and the improved high rate performance for lithium-ion batteries. *Electrochim. Acta* **100,** 125−132 (2013).

[14] Lee, J., Kim, C. & Kang, B. High electrochemical performance of high-voltage $LiNi_{0.5}Mn_{1.5}O_4$ by decoupling the Ni/Mn disordering from the presence of Mn^{3+} ions. *NPG Asia Mater.* **7,** e211 (2015).

[15] Duncan, H., Hai, B., Leskes, M., Grey, C. P. & Chen, G. Y. Relationships between Mn^{3+} content, structural ordering, phase transformation, and kinetic properties in $LiNi_xMn_{2−x}O_4$ cathode materials. *Chem. Mater.* **26,** 5374−5382 (2014).

[16] Zheng, J. et al. Whittingham, M. S. & Zhang, J.-G. Phys. Enhanced Li^+ ion transport in $LiNi_{0.5}Mn_{1.5}O_4$ through control of site disorder. *Chem. Chem. Phys.* **14,** 13515−13521 (2012).

[17] von Cresce, A. & Xu, K. Electrolyte additive in support of 5 V Li ion chemistry. *J. Electrochem. Soc.* **158,** A337−342 (2011).

[18] Xu M.Q. et al. Development of novel lithium borate additives for designed surface modification of high voltage $LiNi_{0.5}Mn_{1.5}O_4$ cathodes. *Energy Environ. Sci.* **9,** 1308−1319 (2016).

[19] Shin, W.-K., Lee, Y.-S. & Kim, D.-W. Study on the cycling performance of $LiNi_{0.5}Mn_{1.5}O_4$ electrodes modified by reactive SiO_2 nanoparticles. *J. Mater. Chem.* **A 2,** 6863–6869 (2014).

[20] Kim, J. W. et al. Surface chemistry of $LiNi_{0.5}Mn_{1.5}O_4$ particles coated by Al_2O_3 using atomic layer deposition for lithium-ion batteries. *J. Power Sources* **274,** 1254−1262 (2015).

[21] Konishi, H. et al. Effect of surface Li_3PO_4 coating on $LiNi_{0.5}Mn_{1.5}O_4$ epitaxial thin film electrodes synthesized by pulsed laser deposition. *J. Power Sources* **269,** 293−298 (2014).

[22] Sachs, M. et al. LiNi$_{0.5}$Mn$_{1.5}$O$_4$ high-voltage cathode coated with Li$_4$Ti$_5$O$_{12}$: a hard X-ray photoelectron spectroscopy (HAXPES) study. *Phys. Chem. Chem. Phys.* **17,** 31790−31800 (2015).

[23] Truong, Q. D., Devaraju, M. K., Tomai, T. & Honma, I. Direct observation of antisite defects in LiCoPO$_4$ cathode materials by annular dark- and bright-field electron microscopy. *ACS Appl. Mater. Interfaces* **5,** 9926–9932 (2013).

[24] Chen, L. et al. Relevance of LiPF$_6$ as etching agent of LiMnPO$_4$ colloidal nanocrystals for high rate performing Li-ion battery cathodes. *ACS Appl. Mater. Interfaces* **8,** 4069−4075 (2016).

[25] Alyoshin, V. A., Pleshakov, E. A., Ehrenberg, H. & Mikhailova, D. Platelike LiMPO$_4$ (M = Fe, Mn, Co, Ni) for possible application in rechargeable Li ion batteries: Beyond nanosize. *J. Phys. Chem. C* **118,** 17426−17435 (2014).

[26] Delacourt, C. et al. Toward understanding of electrical limitations (Electronic, Ionic) in LiMPO$_4$ (M = Fe, Mn) electrode materials. *J. Electrochem. Soc.* **152,** A913−A921 (2005).

[27] Yang, G. et al. The doping effect on the crystal structure and electrochemical properties of LiMn$_x$M$_{1-x}$PO$_4$ (M=Mg, V, Fe, Co, Gd), *J. Power Sources* **196,** 4747−4755 (2011).

[28] Kreder, K.J., Assat, G. & Manthiram, Microwave-assisted solvothermal synthesis of three polymorphs of LiCoPO$_4$ and their electrochemical properties. *Chem. Mater.* **27,** 5543−5549 (2015).

[29] Truong, Q. D., Devaraju, M. K., Ganbe, Y., Tomai, T. & Honma, I. Controlling the shape of LiCoPO$_4$ nanocrystals by supercritical fluid process for enhanced energy storage properties. *Sci. Rep.* **4,** 3975 (2014).

[30] Ni, J., Wang, H., Gao, L. & Lu, L. A high-performance LiCoPO$_4$/C core/shell composite for Li-ion batteries. *Electrochim. Acta* **70,** 349–354 (2012).

[31] Wan, L. et al. Ni/Mn ratio and morphology-dependent crystallographic facet structure and electrochemical properties of the high-voltage spinel $LiNi_{0.5}Mn_{1.5}O_4$ cathode material. *RSC Adv.* **5,** 25988−25997 (2015).

[32] Deng, Y. F., Zhao, S. X., Xu, Y. H., Gao, K. & Nan, C. W. Impact of P-doped in spinel $LiNi_{0.5}Mn_{1.5}O_4$ on degree of disorder, grain morphology, and electrochemical performance. *Chem. Mater.* **27**, 7734−7742 (2015).

[33] Yang, S. F, Chen, J., Liu, Y. J. & Yi, B. L. Preparing $LiNi_{0.5}Mn_{1.5}O_4$ nanoplates with superior properties in lithium-ion batteries using bimetal-organic coordination-polymers as precursors. *J. Mater. Chem. A* **2,** 9322−9330 (2014).

[34] Carabineiro, S. A. C. et al. Carbon monoxide oxidation catalysed by exotemplated manganese oxides. *Catal. Lett.* **134,** 217 (2010).

[35] Rajalakshmi, A. et al. Physicochemical properties of V^{5+} doped $LiCoPO_4$ as cathode materials for Li-ion batteries. *J Sol-Gel Sci Technol.* **65,** 399–410 (2013).

[36] Jian, X.M. et al. Oxalic acid-assisted combustion synthesized $LiVO_3$ cathode material for lithium ion batteries. *J. Power Sources* **246,** 417−422 (2014).

[37] Markevich, E. et al. C. Reasons for capacity fading of $LiCoPO_4$ cathodes in $LiPF_6$ containing electrolyte solutions. *Electrochem. Comm.* **15,** 22–25 (2012).

[38] Yan, G., Li, X., Wang, Z., Guo, H. & Xiong, X. Beneficial effects of 1-propylphosphonic acid cyclic anhydride as an electrolyte additive on the electrochemical properties of $LiNi_{0.5}Mn_{1.5}O_4$ cathode material. *J. Power Sources* **263,** 231−238 (2014).

[39] Philippe, B. et al. Role of the LiPF6 salt for the long-term stability of silicon electrodes in Li-ion batteries − A photoelectron spectroscopy study. *Chem. Mater.* **25,** 394−404 (2013).

[40] Yan, G., Li, X., Wang, Z., Guo, H. & Xiong, X. Beneficial effects of 1-propylphosphonic acid cyclic anhydride as an electrolyte additive on the electrochemical properties of $LiNi_{0.5}Mn_{1.5}O_4$ cathode material. *J. Power Sources* **263,** 231−238 (2014).

[41] Song, Y.-M., Kim, C.-K., Kim, K.-E., Hong, S. Y., Choi, N.-S., Exploiting chemically and electrochemically reactive phosphite derivatives for high-voltage spinel $LiNi_{0.5}Mn_{1.5}O_4$ cathodes. *J. Power Sources* **302,** 22−30 (2016).

**Table 1 | ICP results, physical parameters and the estimated Mn³⁺ percentage.**

	ICP /mol				BET surface area /m² g⁻¹	surface Mn^{3+} percentage /% a)	sum Mn^{3+} percentage /% b)
	Mn	Ni	Co	P			
LNM	1.5	0.48	/	/	6.37	18.1	/
LNM@1%LCP	1.5	0.48	0.011	0.015	5.89	27.0	2.93
LNM@5%LCP	1.5	0.49	0.057	0.039	5.22	34.9	7.87
LNM@10%LCP	1.5	0.47	0.106	0.092	4.80	45.8	14.9

a)(Mn^{3+} ratio calculated by capacity percentage from the 4 V plateau.); b)(Mn^{3+} ratio measured by XPS.)
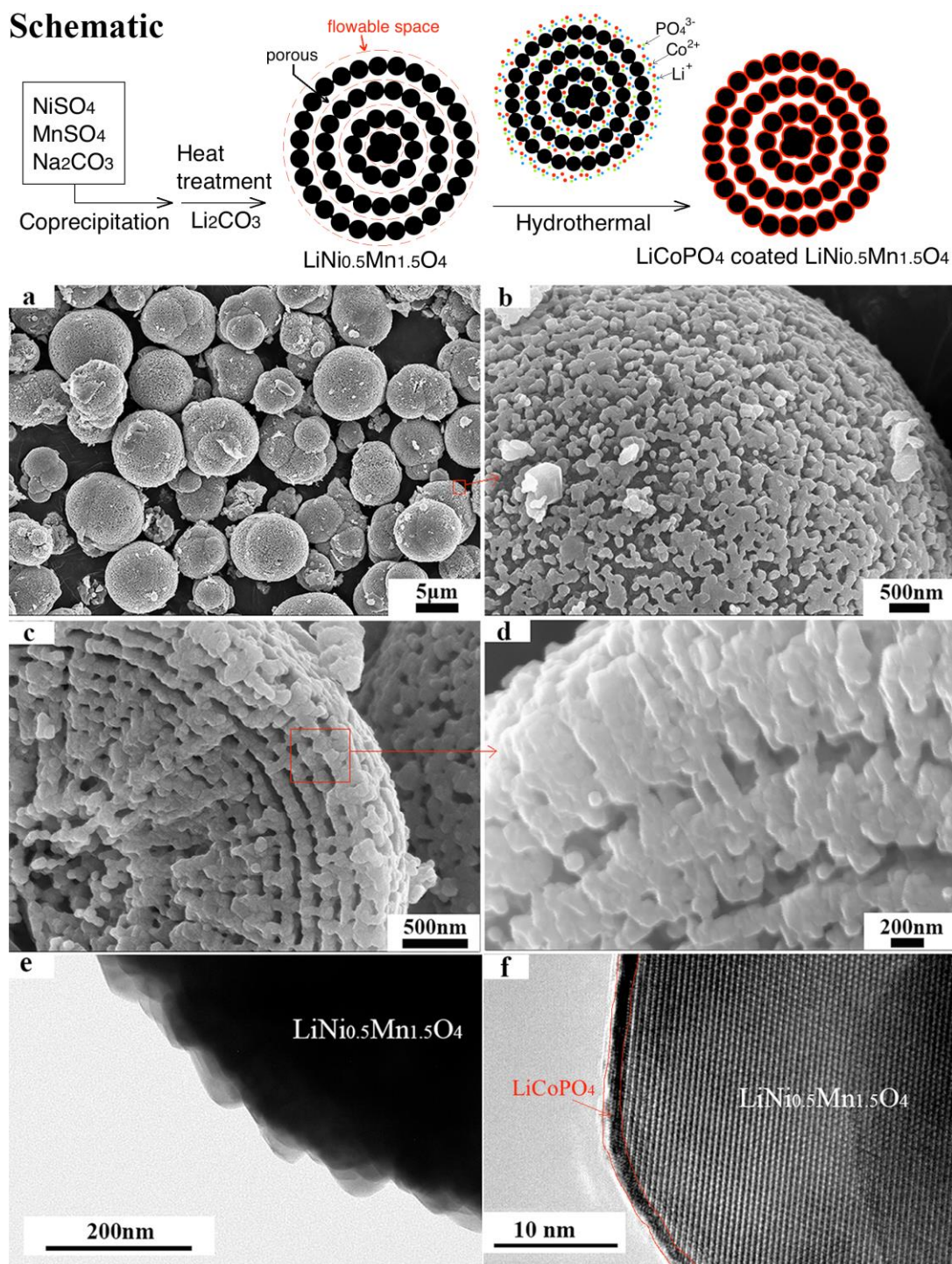
Figure 1 | Schematic of synthesis method and morphology characterization of the LNM@5%LCP. (**Schematic**) Schematic of the preparation route for $LiCoPO_4$ coated $LiNi_{0.5}Mn_{1.5}O_4$; (**a**) SEM images of LNM@5%LCP spherical particles; (**b**) the surface of LNM@5%LCP spherical particles; (**c, d**) the sectional views after the particles were pressed in half; (**e**) TEM image of LNM@5%LCP sample and (**f**) the magnified TEM image.
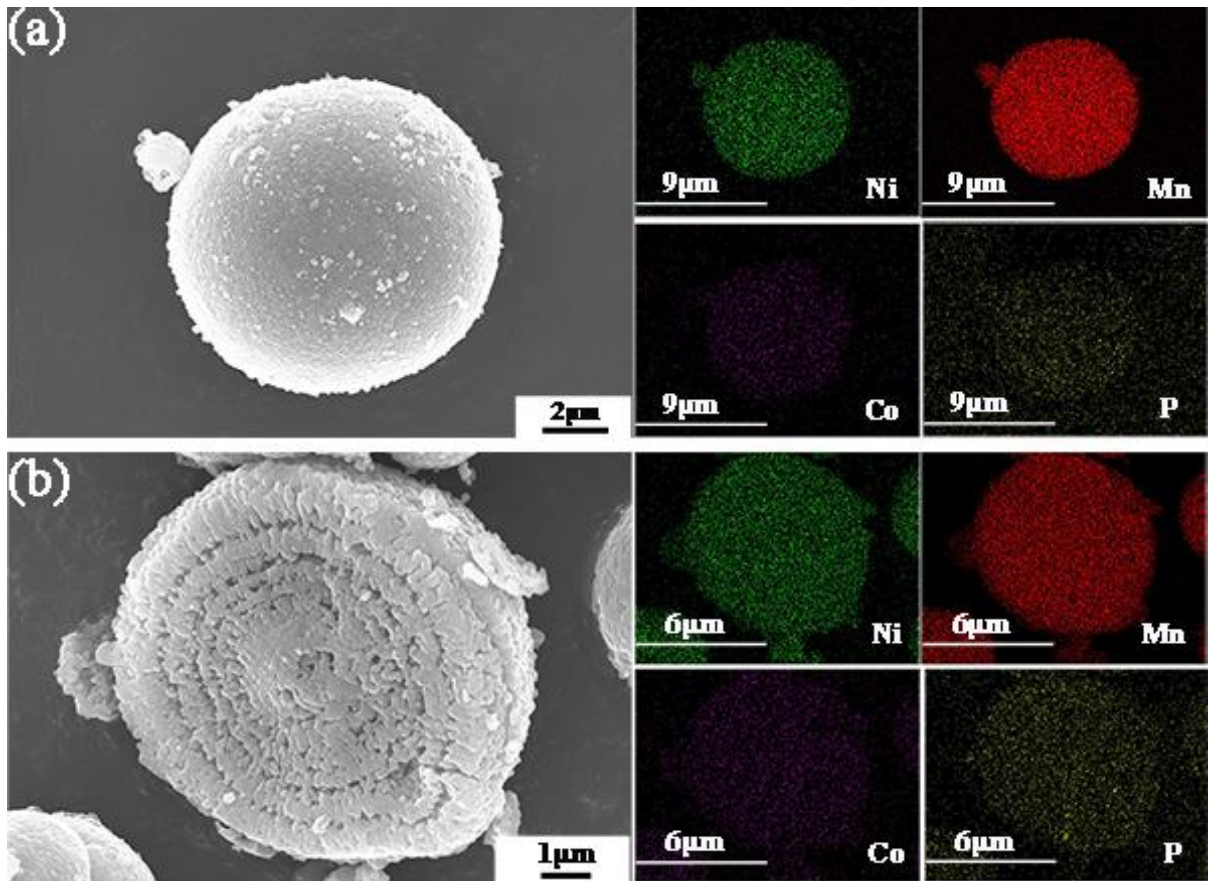
Figure 2 | Element distribution of the LNM@1%LCPO. (**a**) SEM images and the relative EDS mapping in spherical view and (**b**) SEM images and the relative EDS mapping in cross sectional view after the particles were crashed into half.
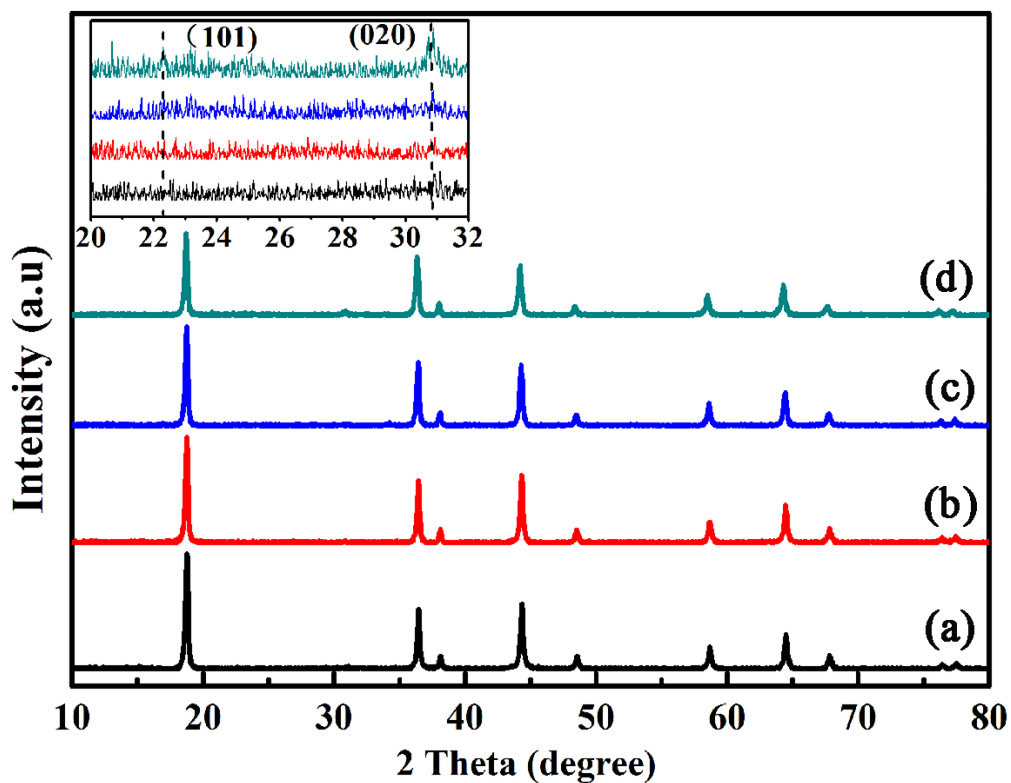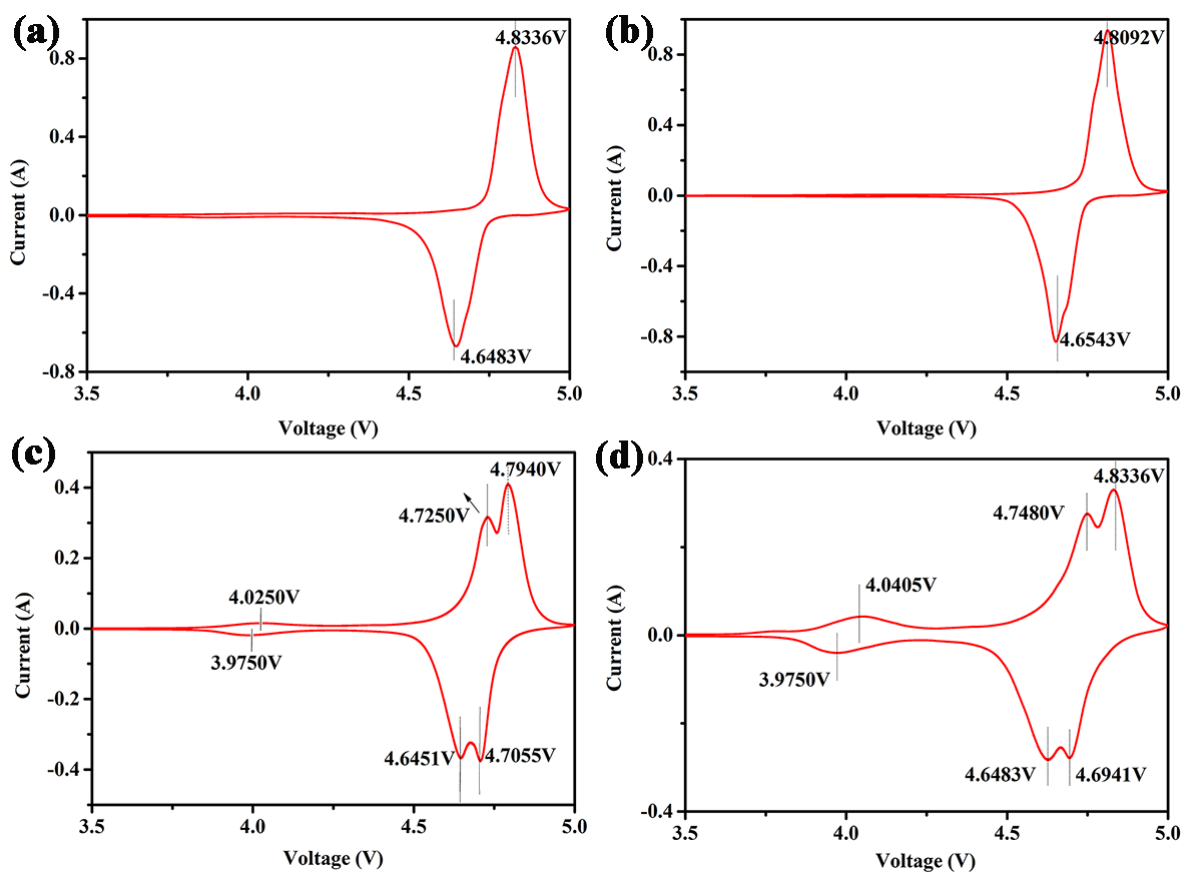
Figure 3 | XRD patterns. (**a**) LNM, (**b**) LNM@1%LCP, (**c**) LNM@5%LCP and (**d**) LNM@10%LCP. The inset: enlarged patterns present the characterized peaks index by LiCoPO$_4$ phase.
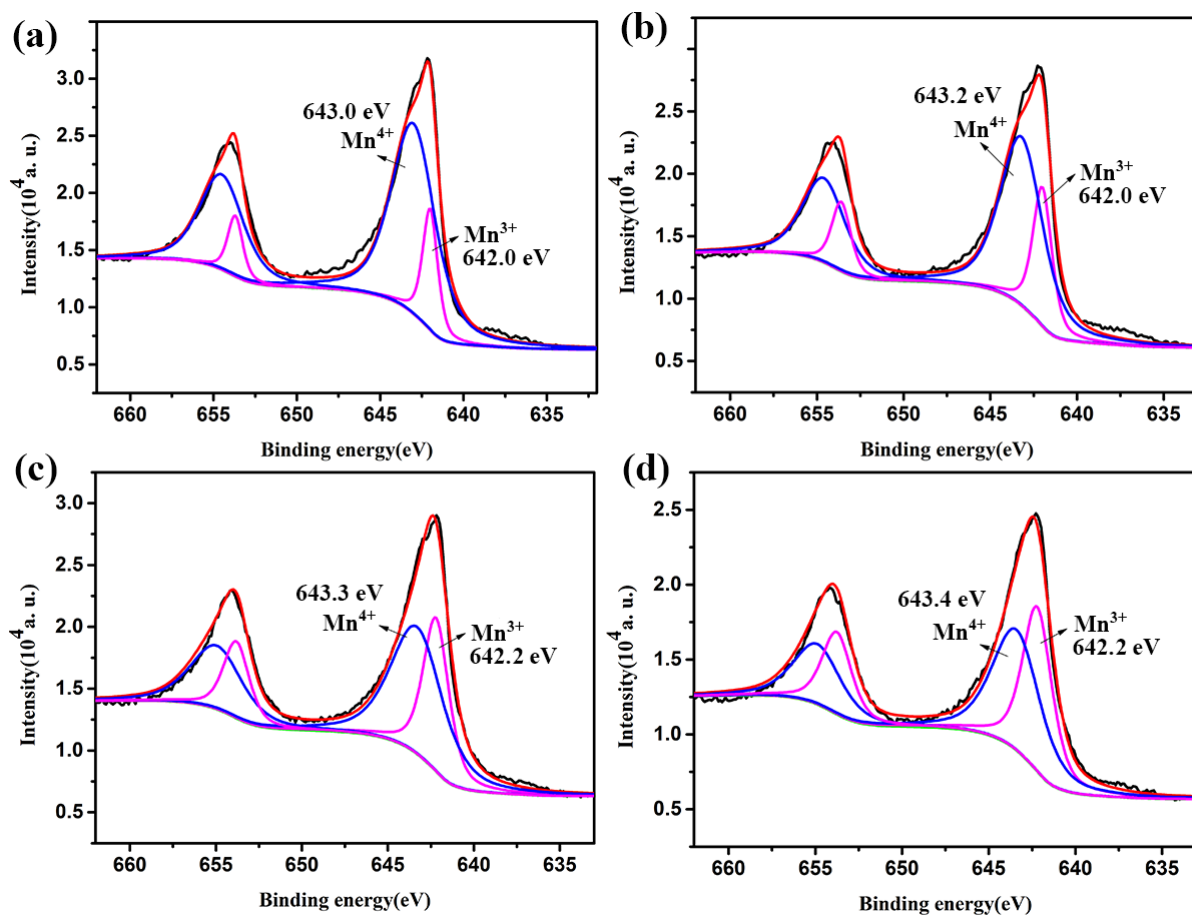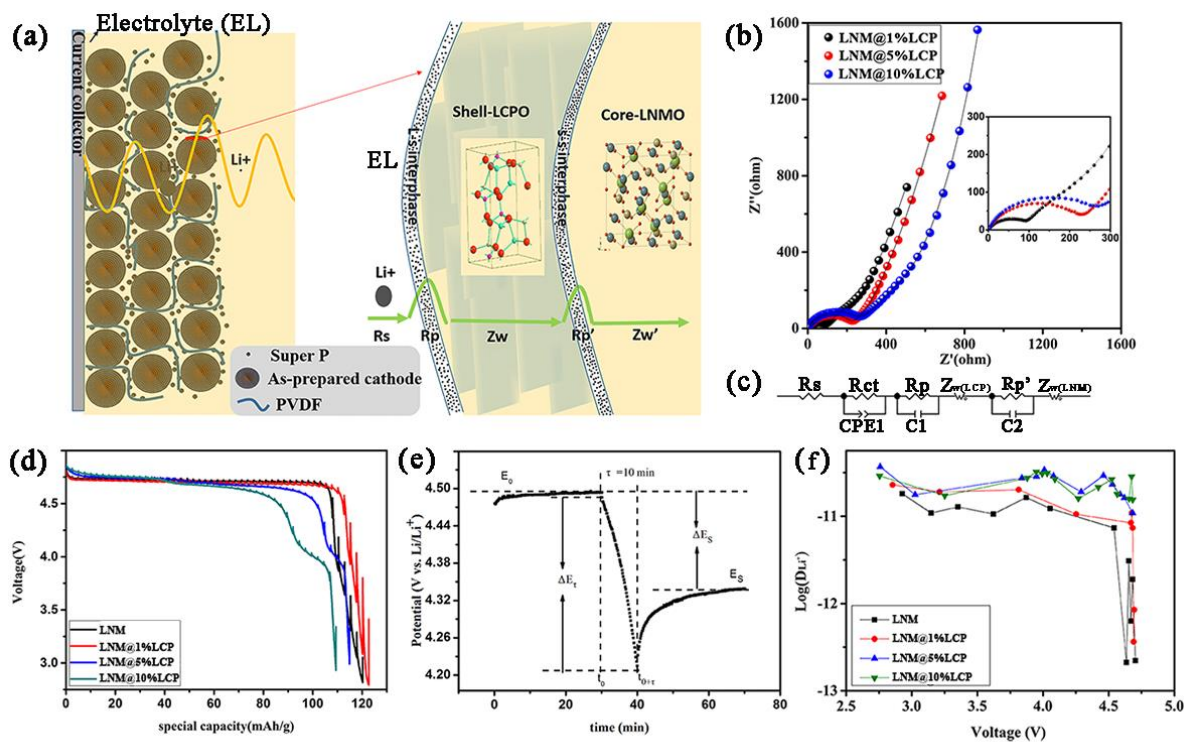
Figure 4 | High resolution XPS spectra in the region of Mn2p. (**a**) LNM, (**b**) LNM@1%LCP, (**c**) LNM@5%LCP and (**d**) LNM@10%LCP, respectively.

Figure 5 | Cyclic voltammograms. (**a**) LNM, (**b**) LNM@1%LCP, (**c**) LNM@5%LCP and (**d**) LNM@10%LCP at a scan rate of 0.1 mV s^{-1}.

Figure 6 | (**a**) A schematic model illustrates the path of Li ions going through LNM@ *x*%LCP, (**b**) Nyquist plots of LNM@1%LCP, LNM@5%LCP and LNM@10%LCP electrodes (inset is the high-frequency region of Nyquist plots) and (**c**) the equivalent circuit, (**d**) GITT curves of the four samples for the fourth discharge between 3 V and 5 V (rate: 0.1 C, time interval: 30 min), (**e**) t vs E profile for a single GITT titration, (**f**) diffusion coefficients of Li$^+$ in LNM, LNM@1%LCP, LNM@5%LCP and LNM@10%LCP, respectively.
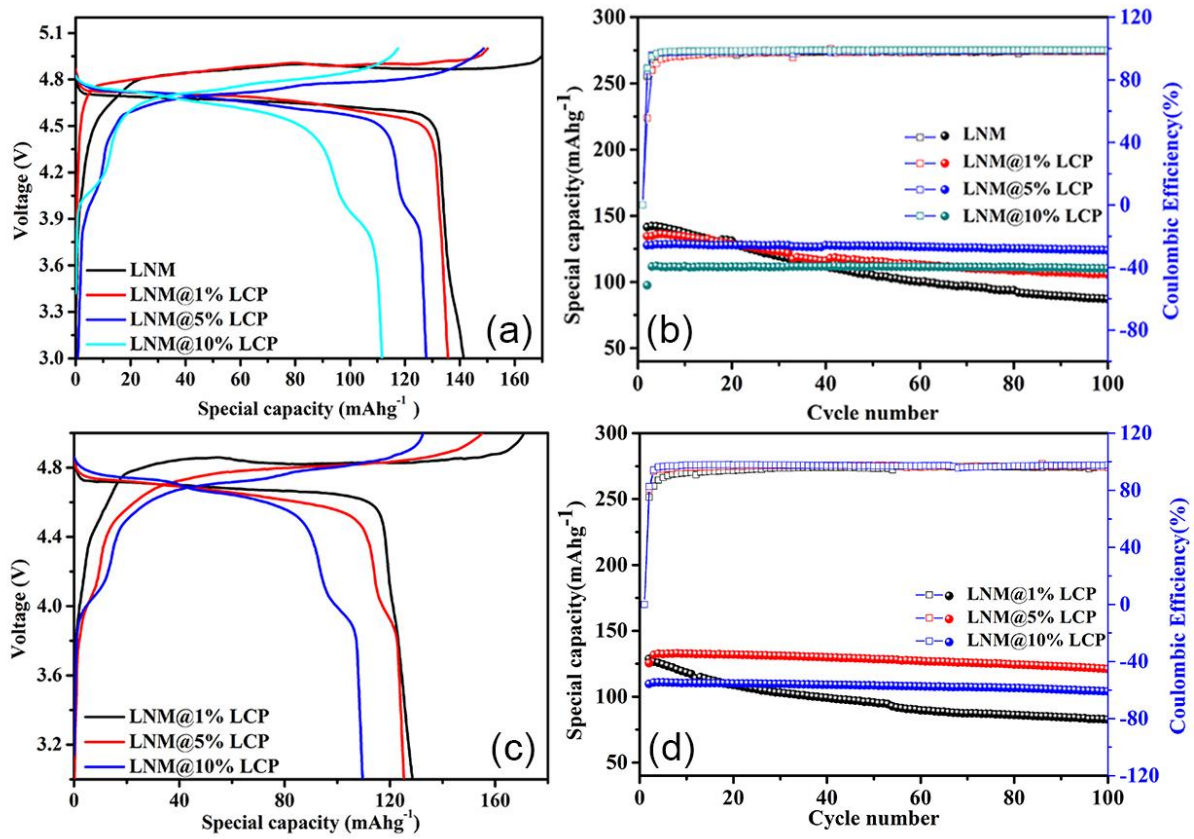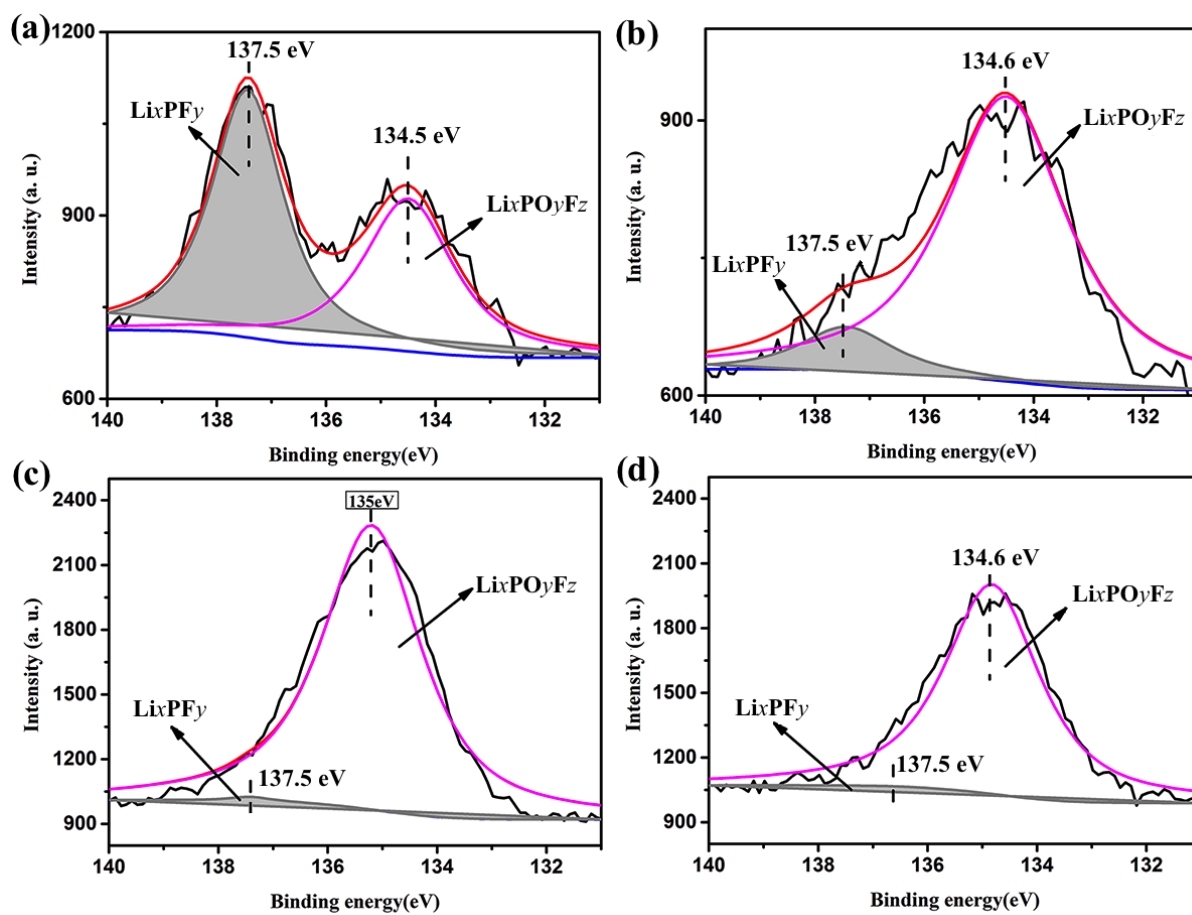
Figure 7 | Initial charge/discharge and cyclic profiles. (**a, b**) at 25 °C and (**c, d**) at 55 °C. The current density is 0.5 C-rate.
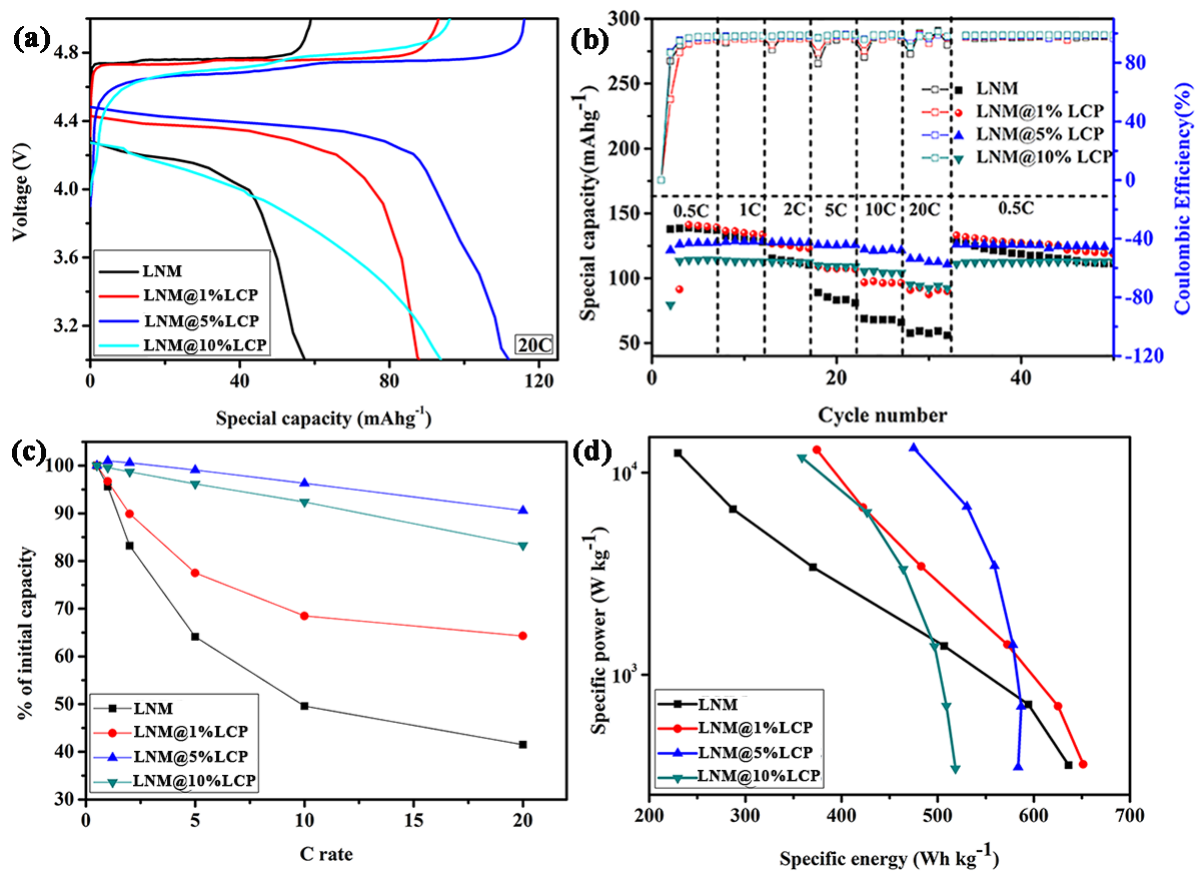
Figure 8 | (**a**) Initial charge/discharge profiles collected at 20 C-rate. (**b**) Rate capability of samples at various C-rates ranging from 0.5 to 20 C. (**c**) Evolution of normalized capacity as a function of discharge rate (**d**) and Ragone plot (d) for the four samples.

Figure 9 | High resolution XPS spectra in the region of P2p taken on the electrodes after 600 cycles at the current rate of 20 C. (**a**) LNM, (**b**) LNM@1%LCP, (**c**) LNM@5%LCP and (**d**) LNM@10%LCP